A Parametric Study on Annular Airfoil Geometry for Collector Electrodes in Electrohydrodynamic Propulsion Systems

Tanay Apte, Varvara Karenski, Mihir Jain

5/15/2026

Tanay Apte, Varvara Karenski, Mihir Jain
Ashland, Massachusetts

Abstract

This project investigates the effect of collector electrode geometry on the thrust of single-stage electrohydrodynamic (EHD) thrusters. EHD thrusters are silent and feature no moving parts, which makes them promising alternatives to small-scale drone propellers. However, their low thrust density remains a major hurdle. A significant contributor to this inefficiency is the aerodynamic drag generated by the collector electrode, which acts against the generated thrust. The thrust was measured using a customized low-friction force measurement setup. Different geometrical parameters of collector electrodes were tested, with a focus on the annular airfoil shape. The thruster was tested with a constant voltage of 8 kV, at a constant electrode gap of 25.4 mm. A negative correlation was observed between thrust and the thickness, camber and convergence angle of the annular airfoil. A net decrease in thrust of up to 32% was measured over the tested parameter ranges. These findings suggest that a slimmer airfoil shape improves aerodynamics and minimizing the collector's aerodynamic profile remains critical for maximizing EHD propulsion efficiency.

Keywords: Electrohydrodynamic thrusters, Ionic wind, Corona discharge, Electric propulsion, Plasma physics, Aerodynamics

Contents

1 Introduction

1.1 Context and Motivation

Electrohydrodynamic thrusters generate thrust by accelerating ions in an electric field and transferring momentum to neutral air molecules. EHD thrusters are enabled by a process called ionic wind, which uses high-voltage electric fields to propel ions, which then collide with neutral air molecules to transfer their momentum. Because they do not have moving parts and operate silently, EHD devices have gained popularity in applications where mechanical simplicity, reduced carbon emissions, and low acoustic signature are desirable. Despite these advantages, current EHD thrusters typically offer a low thrust density, which has limited their practical adoption (Xu et al., 2018). The geometry of the collector electrode presents a challenge in both electrostatics and aerodynamics, since the profile determines the electric field distribution and the aerodynamic drag produced. Current literature has largely focused on the emitter electrode's corona discharge, yet the aerodynamic influence of the collector remains poorly characterized. This study aims to investigate whether streamlined geometric profiles can minimize drag without compromising the electric field strength. A parametric study is conducted to evaluate how variations in parameters of the annular airfoil affect thrust.

1.2 Theoretical Framework of Electrostatic and Fluid interactions

In order to quantify the influence of collector geometry, the physical principles governing electrohydrodynamic thrust and aerodynamic resistance must be established. The net thrust of the EHD propulsion system is defined as:

$$F_{net} = F_{EHD} - F_D \tag{1}$$

Where F_{EHD} is the force associated with ion-neutral momentum transfer and F_D is the aerodynamic drag of the collector electrode

Assuming total ion-neutral momentum transfer, the EHD force generated by the thruster can be expressed as the volume integral of the electric body force over the discharge region:

$$F_{EHD} = \int_{\mathscr{V}} \rho_q E \, d\mathscr{V} \tag{2}$$

where ρ_q is the local charge density and E is the electric field at each point within the electrode gap. Assuming steady ion drift and approximating the electric field and charge density as uniform within the active discharge region, the integral reduces to

$$F_{EHD} \approx \rho_q E \int_{\mathscr{V}} d\mathscr{V} \tag{3}$$

$$F_{EHD} \approx \rho_q E \mathscr{V} \tag{4}$$

where $\mathscr{V}$ denotes the volume of the discharge region. Approximating this region as having effective cross-sectional area A and gap length d, such that $\mathscr{V} = Ad$, yields

$$F_{EHD} \approx \rho_q EAd \tag{5}$$

The ionic current is given by

$$I = \rho_q v_D A \tag{6}$$

where v_D is the ion drift velocity and A is the effective cross-sectional area of flow. Solving for charge density,

$$\rho_q = \frac{I}{v_D A} \tag{7}$$

The ion drift velocity is related to ion mobility and electric field by $v_D = \mu E$. Substituting into the charge density expression gives

$$\rho_q = \frac{I}{\mu EA} \tag{8}$$

Substituting into the thrust equation,

$$F_{EHD} = \frac{IEAd}{\mu EA} \tag{9}$$

Which simplifies to

$$F_{EHD} \approx \frac{Id}{\mu} \tag{10}$$

This expression relates thrust to the ionic current I, electrode separation d, ion mobility μ under the stated uniform-field and negligible diffusion. For corona discharge, current is modeled by the Townsend Relation as:

$$I = KV(V - V_0) \tag{11}$$

Where V is the applied voltage and V_0 is the corona onset voltage dependent on the emitter's geometry. The proportionality constant K reflects the global electrode configuration and field distribution, and is therefore dependent on both emitter and collector geometry. Since $F \propto I$, and $I \propto K$, collector geometry affects the electric field distribution.

To account for the influence of collector geometry on net performance, the electrostatic

thrust is combined with the aerodynamic drag force acting on the collector, modeled here using a standard drag model. For a streamlined body in incompressible flow, the drag force is:

$$F_D = \frac{1}{2}\rho_{air} v_{air}^2 C_D A_f \tag{12}$$

Where ρ_{air} is air density, v is airflow velocity, C_D is the drag coefficient of the collector, and A_f is the frontal area of the collector. v is assumed to be the average velocity of neutral molecules assuming uniform momentum transfer.

The drag force is proportional to the drag coefficient and frontal area, which are both dependent on collector geometry. The drag coefficient is a function of the flow's Reynolds number (Re). The Reynolds number characterizes the ratio of inertial forces to viscous forces within the fluid:

$$Re = \frac{\rho_{air} v L}{\eta_{visc}} \tag{13}$$

Where L is the characteristic length (in this case, the chord length of the collector), and η_{visc} is the dynamic viscosity of air. Assuming an average air velocity range between 1 to 4 meters per second, $1500 < Re < 8000$. The airflow remains in a laminar-to-transitional range, predicting that the frontal area will have a substantial effect on drag.

To obtain a self-consistent expression for net thrust, the induced airflow velocity must be related to the generated electrohydrodynamic force. Under steady conditions, thrust equals the rate of momentum imparted to the air,

$$F_{EHD} = \dot{m} v_{air} \tag{14}$$

Where $\dot{m}$ is the mass flow rate of air through the discharge region. Assuming incompressible flow and uniform velocity across an effective cross-sectional area A, the mass flow rate may be expressed as

$$\dot{m} = \rho_{air} A v_{air} \tag{15}$$

Equating this with the previously derived thrust relation gives

$$\frac{Id}{\mu} = \rho_{air} A v_{air}^2 \tag{16}$$

Solving for the induced airflow velocity,

$$v_{air} = \sqrt{\frac{Id}{\mu \rho_{air} A}} \tag{17}$$

Substituting into the drag model:

$$F_D = \frac{1}{2}\rho_{air}\left(\frac{Id}{\mu\rho_{air}A}\right)C_D A_f \tag{18}$$

Canceling ρ_{air} gives

$$F_D = \frac{1}{2}\frac{Id}{\mu A}C_D A_f \tag{19}$$

By substituting the derived expressions for ion-driven momentum transfer and the drag model for a body in a fluid stream,

$$F_{net} = \frac{Id}{\mu} - \frac{1}{2}\frac{Id}{\mu A}C_D A_f \tag{20}$$

We can factor out the common term $\frac{Id}{\mu}$ to arrive at the governing equation for the thruster:

$$F_{net} = \frac{Id}{\mu}\left(1 - \frac{C_D A_f}{2A}\right) \tag{21}$$

Where I is current, d is electrode gap, μ is ion mobility, C_D is drag coefficient of the collector electrode, A_f is frontal area of the collector electrode, and A is the cross-sectional area of momentum transfer. This equation is derived under the simplifying assumptions of uniform charge density and electric field, complete ion-neutral momentum transfer, negligible ion recombination and diffusion, constant ion mobility, and uniform airflow velocity across the effective cross-sectional area. This equation is not a predictive calculation; it represents a conceptual framework to demonstrate scaling relationships qualitatively.

1.3 Literature Review

Due to the ongoing development of electrohydrodynamic plasma propulsion as a field, limited research has explored on the effects of collector electrode geometry on net thrust. However, investigations assessing the effects of other variables on system efficiency and thrust generation have been conducted.

Drew & Pister (Drew & Pister, 2017) conducted an analysis of the geometry of wire-needle and grid electrodes within electrohydrodynamic thrusters, particularly the effects of electrode tip angle on current generation and plasma localization. A key finding of their study was a significant correlation ($p = 0.01$) between the number of electrode tips and the Corona Inception Voltage (C). Conversely, Drew & Pister observed no significant effect of emitter electrode spine height on either the inception voltage or resulting discharge current. Their research provides a foundation for the geometric optimization of EHD electrodes and concludes that electrode geometry is vital to the maximization of a system's thrust. Notably, the authors concluded that decreasing the electrode gap distance increased the thrust loss factor by approximately

30%, highlighting the intricate yet unexplored balance required between compact design and aerodynamic efficiency. The deduction by Drew and Pister that ”positive corona discharge is primarily driven by geometry” serves as a key confirmation for this research. This study holds the number of emitter spikes and the electrode gap constant, allowing for a concise analysis of the varying effects of collector electrode geometry. While Drew and Pister delved into the effects of voltage and grid-style electrode geometries on thrust, their analysis did not extend to cylindrical electrode configurations.

An analysis of EHD propulsion devices (Masuyama, 2012) authored by Kento Masuyama provides further insight into the effects of electrode geometry on the performance of electrohydrodynamic (EHD) thrusters. His research supports the previously determined conclusion that an increase in system voltage yielded an increase in thrust produced. A critical observation in this work is that increasing the electrode gap distance raises the voltage threshold for thrust onset but simultaneously enhances efficiency, generating ”more thrust per input power.” Notably, Masuyama’s research reports that a thrust-to-power ratio as high as 68.43 mN/W was obtained for a thruster with an electrode gap of 21 cm. An integral claim by Masuyama states that an unexplored part of EHD propulsion that must be studied includes ”how much losses are induced from neutral particles colliding with the additional surface area of electrodes.”

Modeling of Electrohydrodynamic (EHD) Plasma Thrusters, by (Calvo, Pinheiro, & Sá, 2022) similarly investigates the effects of cathode geometry on EHD thruster output. Though their research involves gas-facilitated EHD propulsion, they have nonetheless introduced the crucial concept that the collector electrode’s geometry holds a particular significance to the function of an EHD system as a whole. Their findings reported measured optimal cathode width in EHD thrusters supplied with Argon to be 12mm, as any other variation, upper or lower, would decrease the output thrust and the thruster efficiency. The team’s experiments with xenon concluded that the optimal hollow radius was 20 mm, providing the best thrust and thruster efficiency. While Calvo et al. experimented with variables such as hollow radius, cylindrical height, and secondary electron emission coefficient, they did not include parameters of an aerodynamically streamlined body.

While previous studies, such as those by (Kahol, Belan, Pacchiani, & Montenero, 2023), have established scaling relations for wire-to-airfoil configurations, these findings are primarily optimized for airfoil-shaped electrodes. Kahol et al. demonstrate that while increased electrode thickness increases generated thrust, it simultaneously incurs a ’drag penalty’ by disrupting airfoil aerodynamics. Considering the observed effects of collector electrode chord and thickness on EHD propulsion systems, Kahol et al.’s research determines that electrode morphology and the resulting aerodynamics are critical to the performance of EHD systems. This investigation also supports the premise that the optimization of electrode geometry will further studies of

EHD thruster efficiency.

In an investigation of electrohydrodynamic thrust density, (Gilmore & Barrett, 2015) researchers characterized the critical relationship between wire emitter gauge and corona discharge stability. They found that wires larger than 0.2.mm resulted in accurate fabrication and thrust measurement, but sufficiently large emitter electrodes "fail to result in corona inception." This relationship implies that electrode geometry dictates system output; specifically, insufficient corona discharge inherently limits resulting thrust. Perfecting electrode design electrode architecture is a significant step toward developing functional EHD thrusters. While Gilmore and Barrett provide a comprehensive analysis of the emitter's role in thrust production regarding the effects of emitter electrode geometry on the thrust of EHD thrusters, their research does not explore the effects of varied collector electrode geometries.

1.4 Research Gap

The current literature on EHD propulsion remains weighted toward the parametric characterization of the emitter electrode, specifically concerning the influence of corona wire curvature on ionic wind velocity. Current experimental frameworks prioritize the voltage-thrust scaling laws while treating the collector as a passive reservoir to neutralize ions. Consequently, investigating collector electrode aerodynamics represents a necessary advancement in the field. While research has begun incorporating streamlined architectures like annular airfoils, the performance characteristics of these geometries remain under-examined. This is largely attributable to the high degree of nonlinear coupling between electrostatic fields and fluid dynamics, which complicates the possibility of a simplified analytical modeling to develop precise scaling relationships. An experimental study on the trade-off between electrostatic and aerodynamic optimization is conducted to determine their effects on thruster performance. Considering the existing conclusions that the aerodynamics of electrodes and geometrical optimization are crucial to optimizing the performance of a system, our research seeks to understand the relationship between an EHD propulsion system's collector electrode thickness, camber, and convergence angle and output thrust.

2 Objectives and Variables

2.1 Objectives and Limitations

The primary objective of this study is to conduct an experimental parametric analysis of collector airfoil geometries to determine their influence on the net thrust of a single-stage EHD thruster. The study aims to identify geometric trends and parameter ranges that maximize absolute thrust under fixed operating conditions; efficiency and thrust-to-power ratios are not considered. This characterization is limited to specific geometric ranges and does not claim global optimization of an ideal electrode geometry.

2.2 Variables

Within the context of this study, the emitter electrode is ring-shaped with sawtooth spikes in order to reduce corona onset voltage and increase electric field intensity. The collector electrode, featuring a cylinder with an airfoil cross-section, is located axially downstream of the emitter. The parameters of the collector electrode geometries are varied, while the emitter-collector separation and emitter geometry are kept constant.

This investigation studies three independent geometric parameters:

- Airfoil Thickness, defined as a percentage of the chord length
- Airfoil Camber, defined as a percentage of the chord length, representing the depth of the curve of the airfoil
- Convergence Angle, defined in degrees from the central axis, representing the radial convergence of the nozzle created from the ring

Airfoil Thickness and Camber are identified using 4-series NACA Numbers. For instance, the control electrode is designated as a NACA 0024 profile, indicating 0% camber, 0% camber position, and a 24% thickness-to-chord ratio. Camber position is maintained to be 30% of the chord length for all cambered airfoils.

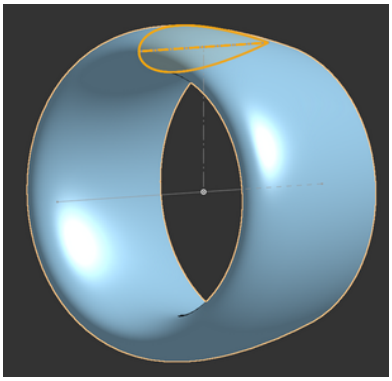

Figure 1: Control electrode: 0024, 0° convergence angle

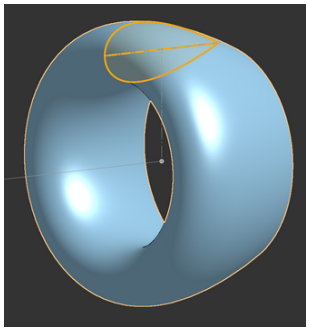

(a) Maximum thickness: 0040

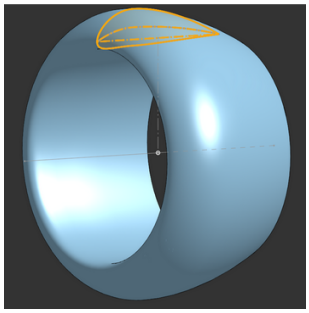

(b) Maximum camber: 8324

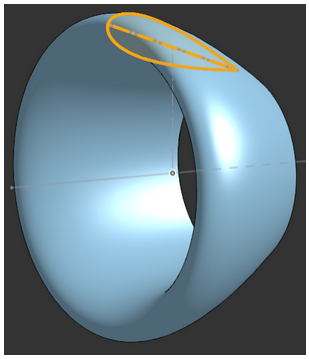

(c) Maximum convergence angle: 20°

Figure 2: Visualization of maximum collector electrode geometries

2.3 Hypotheses

Based on predicted influence of collector electrode geometry on ion collection and aerodynamic drag, the following hypotheses were formulated for each geometric parameter.

1. Airfoil Thickness: Increasing collector airfoil thickness will reduce net thrust due to higher aerodynamic drag from increased frontal area.

2. Airfoil Camber: Moderate positive airfoil camber will increase thrust due to mass flow entrainment through the Coandă Effect, while excessive camber will decrease thrust due to flow separation and increased frontal area.

3. Convergence Angle: Increasing the collector convergence angle will increase thrust by reducing the cross-sectional area of flow to further accelerate the air. Thrust will decrease past a certain threshold beyond which the increase in frontal area causes significant aerodynamic drag and the decrease in exit area causes back pressure.

3 Methods

3.1 Lab Setup

This research required the design of an experimental system in order to operate the thruster and facilitate data collection. The apparatus is comprised of three primary subsystems: a high-voltage power source, a force measurement assembly, and a data acquisition (DAQ) system.

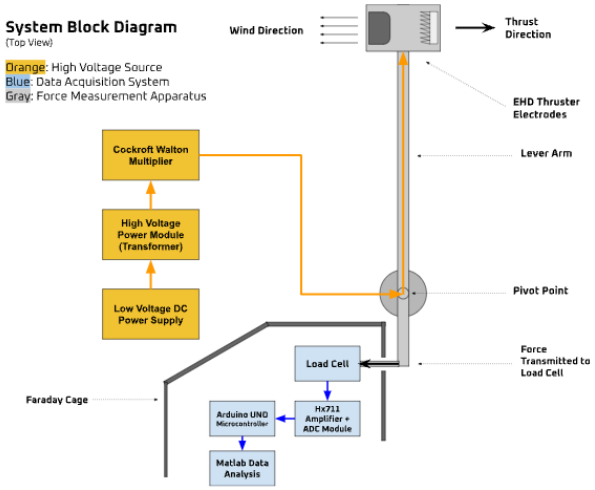

Figure 3: A block diagram of the system integration

3.1.1 High Voltage Power System

The thruster was powered by a regulated DC supply that provided a constant 10 V input. This low-voltage input was fed into a high-voltage step-up transformer module, producing an intermediate potential of approximately 3 kV. The transformer output was then connected to a Cockcroft–Walton voltage multiplier stage to generate the final high-voltage output applied to the emitter electrode. The collector electrode was maintained at ground potential.

Voltage was calculated using a high-resistance divider network and scaled according to the divider ratio. A voltage of approximately 80 volts was measured over R_2 in a voltage divider of $R_1 = 14000\text{k}\Omega$ and $R_2 = 141\text{k}\Omega$. The applied voltage (V_{in}) was derived using the standard voltage divider relationship:

$$V_{in} = V_{out}\left(\frac{R_1 + R_2}{R_2}\right) \tag{22}$$

$$V_{in} = 80\text{ V} \times \left(\frac{14000\text{ k}\Omega + 141\text{ k}\Omega}{141\text{ k}\Omega}\right) \approx 8\text{ kV} \tag{23}$$

Because the corona discharge presents a dynamic and load-dependent impedance, the measured divider voltage provided only an approximate indication of the operating potential, due to voltage drop from the Cockcroft-Walton multiplier.

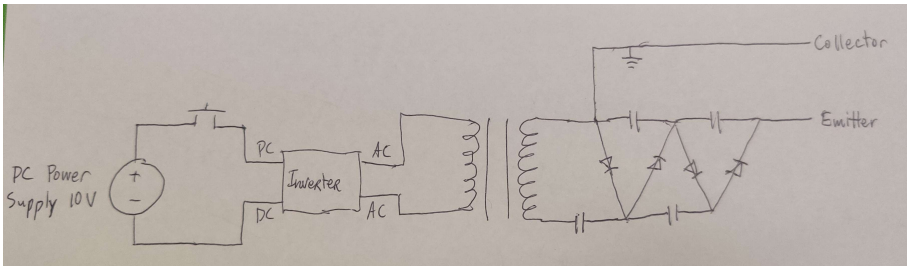

Figure 4: Circuit Diagram

3.1.2 Force Measurement Apparatus

The thrust generated by EHD propulsion is measured by millinewtons (mN), and the commercial load cell used in this experiment did not feature sufficient signal-to-noise ratio (SNR) to reliably measure such forces. The force generated by the thruster required amplification to increase the SNR. In order to facilitate this mechanical advantage, the experimental setup included a horizontal lever with a 6:1 ratio. The lever had one degree of freedom around a vertical yaw axis, negating the effect of gravity on the load cell's measurements. The electrodes were placed on one side, while the opposite side transferred force onto the cantilevered load cell using a rigid pushrod. During steady-state operation, the standard deviation of the thrust signal over a temporal domain was approximately 5 percent of the mean measured thrust, indicating reasonable measurement stability. The wires supplying voltage to the thruster were coaxially routed through a tube on the pivot point of the lever such that the wires would not exert a torsional force on the lever.

The lever consisted of two wooden push dowels spanning the length between the pushrod, rigid pivot point, and electrode mount. A ball bearing degreased with 98% isopropyl alcohol was used to minimize static friction along the pivot point.

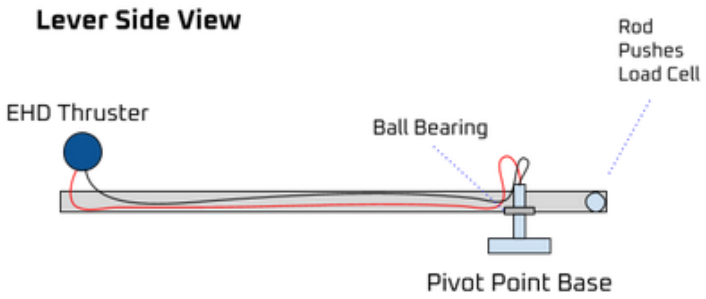

Figure 5: Lever with thruster mounted

3.1.3 Data Acquisition System

The primary components for data acquisition were a 5 kg Wheatstone bridge load cell paired with a 24-bit HX711 amplifier and analog-to-digital converter (ADC). The ADC was connected to an Arduino UNO microcontroller board which relayed the data to MATLAB which was

used to perform data analysis. The microcontroller was physically elevated to reduce the risk of high-voltage surface leakage or tracking along nearby surfaces. The millivolt-range wires between the load cell and the amplifier were wrapped in a grounded aluminum foil shield to prevent electrostatic charges and electromagnetic interference (EMI) from disrupting the data. A grounded Faraday cage was constructed from cardboard and aluminum foil as a continuous conductive enclosure to protect the data acquisition system from EMI from the HV generator. A star ground plane was used as a common ground reference and was connected to earth ground.

Data acquisition was automated via MATLAB and C++ scripts, triggered by a tactile button input on the Arduino controller. Each test cycle lasted 30 seconds and was divided into three distinct phases:

1. Baseline Calibration (0–10s): With the thruster inactive, the system recorded the average load cell output to establish a zero-reference baseline. This accounted for residual sensor offset and minor calibration errors.

2. Stabilization Period (10–20s): The thruster was activated; however, data analysis was suspended to allow the system to reach a steady state. This delay prevented measurement inaccuracies caused by transient spikes or the initial mechanical impact of the lever arm against the load cell.

3. Thrust Measurement Phase (20–30s): The final 10 seconds of steady-state thrust were averaged.

The net thrust was determined by subtracting the initial baseline average from the final measurement average, then dividing by the lever ratio. For each test, standard deviation of the Thrust Measurement Phase was confirmed to be less than 5 percent of the average thrust to mitigate error from corona discharge instability, or the test was repeated.

3.2 Electrode Fabrication

The collector electrodes were designed as NACA 4-series airfoils, with the NACA 0024 (0 degree convergence angle) designated as the control geometry. Each collector maintained a chord length of 25.4 mm and a mid-chord diameter of 38.1 mm. The electrodes were designed using an airfoil profile generator script within the Onshape CAD software. The physical models were 3D printed in PLA and rendered conductive through the application of three coats of copper-based paint. The copper paint was applied uniformly to mitigate electric field inconsistencies and upstream corona discharge from the collector's surface roughness and 3D print layers.

3.3 Experimental Procedure

The load cell was calibrated prior to testing using a known 50 gram weight to establish the force conversion factor. To ensure measurement accuracy before each experimental trial, the

load cell output was tared to eliminate residual offset or drift from previous measurements.

Data acquisition was initiated by executing the custom MATLAB script, which established serial communication with the microcontroller and began real-time data logging and plotting of the load cell output. An initial baseline period of 10 seconds was recorded prior to energizing the high voltage supply to record steady-state zero conditions. Following this baseline interval, the high voltage supply was activated and operated for the remainder of the programmed acquisition window.

Following each trial, raw measurement data was exported and stored in *.csv* format for subsequent analysis. The time-averaged thrust value was computed from the recorded data. After each test, the electrodes were intentionally discharged to ensure safe handling and eliminate residual electrical potential.

Each electrode was tested with 8 trials, and all trials were organized in rotational cycles such that all configurations were tested once before any single configuration was repeated. This structured rotation was implemented to mitigate the influence of thermal effects, and time-dependent system drift on the comparative results.

Respirators with NIOSH-Approved Filters were worn throughout testing to provide protection from the low-concentration byproduct ozone produced by the thruster. This ozone was vented out of the testing area following each test.

3.4 Statistical Methods

In order to facilitate data analysis, the values of thrust were graphed in relation to their collector electrode geometries, and a line of best fit was used to interpret data trends. The trend line was selected out of possible linear, quadratic, and exponential fits through R^2 comparison. In order to prevent overfitting, higher degree polynomial fits were avoided. Graphs also display a piecewise mean-connect line to represent change in average thrust. All graphs were created using MATLAB. A single-variable ANOVA was used to assess each variable for trend significance based on p-value, with a significance threshold of $p = 0.05$.

3.4.1 Normalization

It is important to note that testing was conducted over multiple days. Atmospheric conditions may have affected total thrust across multiple rotations, although conditions were constant for each rotation. To account for this, the baseline thrust difference of all data points in each rotation relative to the thrust of their control geometry was calculated. The normalized relative thrust was graphed and analyzed using a single-variable ANOVA to isolate the effects of differing collector electrode geometry.

4 Results

4.1 Thickness

Experimental data indicated that increasing collector electrode thickness decreased net thrust, as seen in Figure 6. From electrode 0024 to electrode 0040, average thrust decreased from ∼3.6 mN to ∼3.0 mN. From electrode 0024 to 0016, average thrust increased from ∼3.6 mN to 4.3 mN. Statistical analysis using a one-way ANOVA yielded $p \approx 0.056$, failing to reject the null hypothesis regarding thickness and total non-normalized thrust.

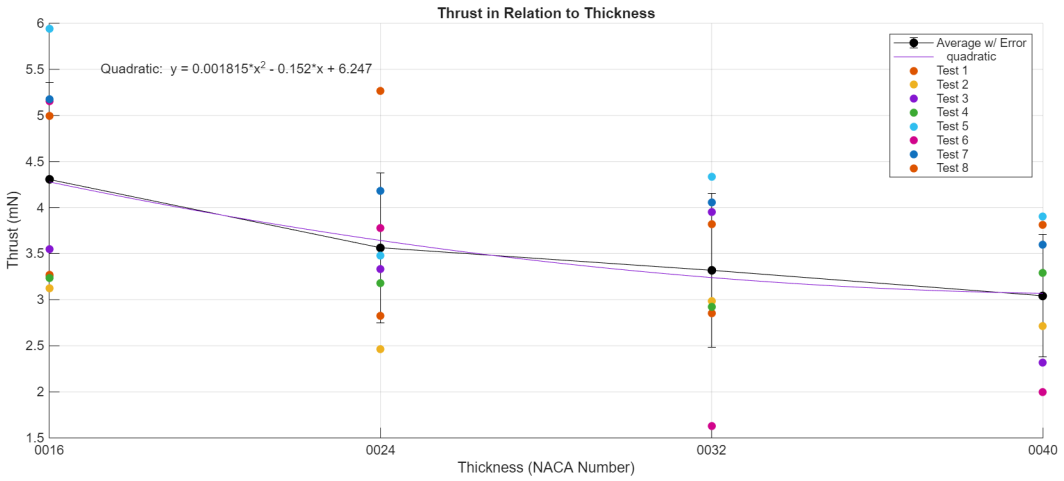

Figure 6: Total thrust vs thickness.

Figure 7 shows the calculated change in thrust from the control geometry relative to the thickness. Statistical analysis using a one-way ANOVA yielded $p \approx 0.023$, demonstrating that the normalized relative thrust was strongly affected by the thickness.

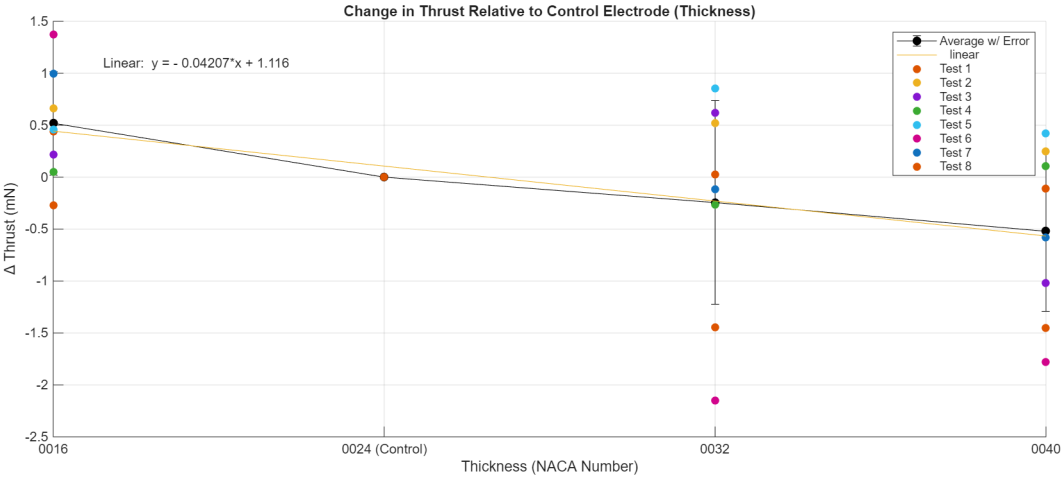

Figure 7: Normalized relative thrust vs thickness.

This demonstrates that the relation between normalized relative thrust and thickness is statistically significant within this range.

4.2 Camber

The experimental data indicates that the camber of the collector electrode significantly influences thrust. From electrode 0024 to electrode 8324, the average thrust decreased from ∼4.75 mN to ∼3.4 mN. An increase in camber resulted in a pronounced decrease in net thrust as seen in Figure 8, a trend confirmed by ANOVA to be highly significant ($p \approx 0.040$). Consequently, the null hypothesis regarding collector camber and total non-normalized thrust is rejected.

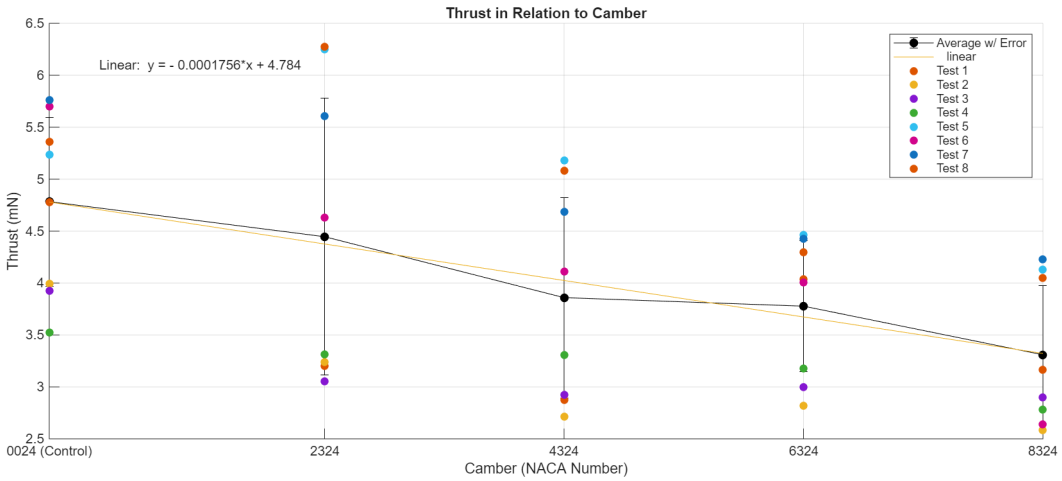

Figure 8: Total thrust vs camber.

Figure 9 shows the calculated change in thrust from the control geometry relative to the camber. Statistical analysis using one-way ANOVA yielded $p \approx 3.46 \times 10^{-4}$, demonstrating that the normalized relative thrust was significantly affected by the camber.

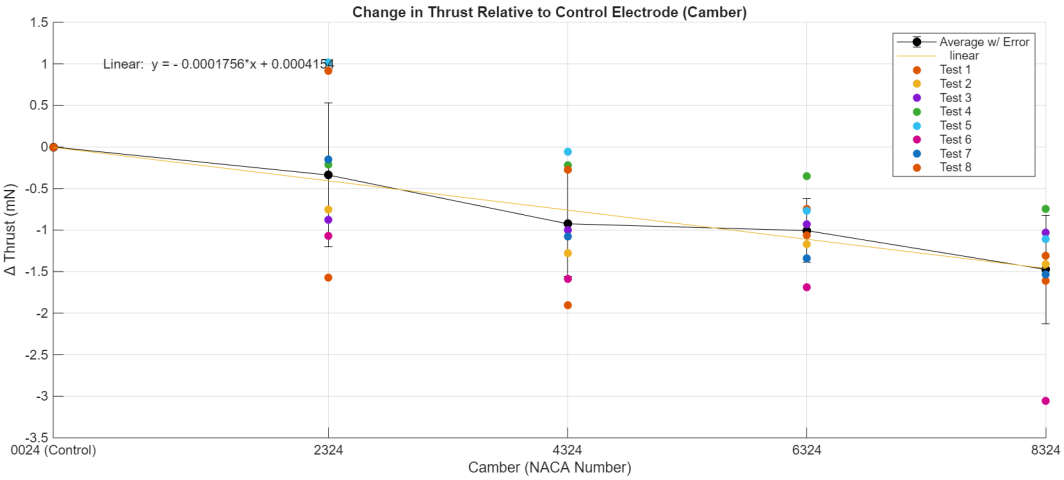

Figure 9: Normalized relative thrust vs camber.

This demonstrates that the relation between normalized relative thrust and camber is statistically significant within this range.

4.3 Convergence Angle

Experimental data revealed that the collector electrode's convergence angle does not significantly influence total non-normalized thrust. A one-way ANOVA refuted the statistical significance of this trend with $p \approx 0.18$, preventing the rejection of the null hypothesis. From convergence angle 0 degrees to 20 degrees, average thrust decreased from ∼4.3 mN to ∼3.5 mN. A downward trend in Figure 10 is visible, showing a slight decrease in thrust with an increase in convergence angle.

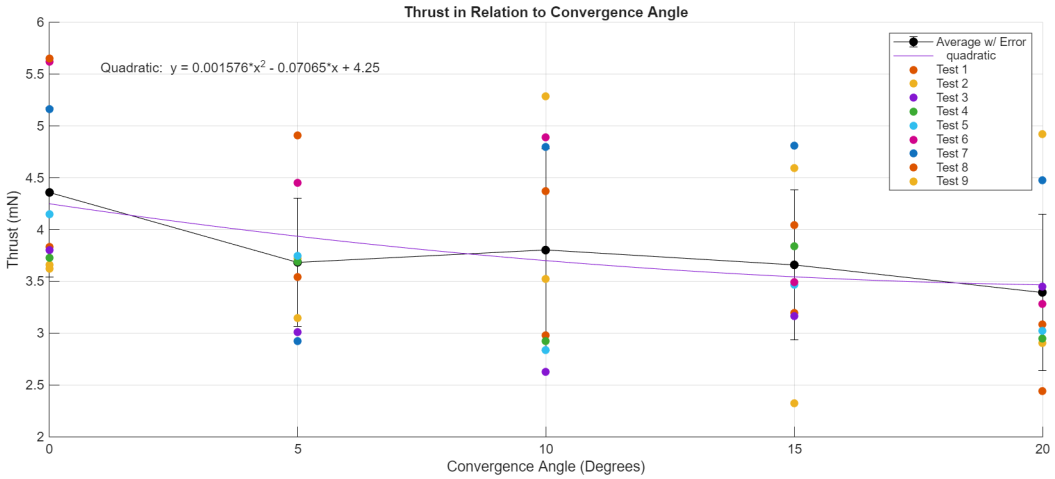

Figure 10: Total thrust vs convergence angle.

Figure 11 illustrates the calculated change in thrust from the control geometry relative to the convergence angle. Statistical analysis using one-way ANOVA yielded $p \approx 0.0028$, demonstrating that normalized relative thrust was affected by the convergence angle.

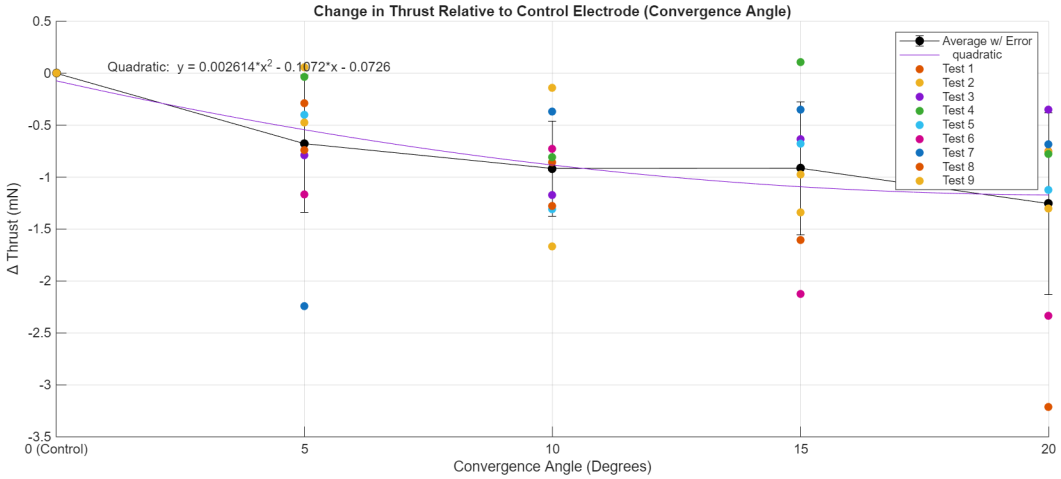

Figure 11: Normalized relative thrust vs convergence angle.

This demonstrates that the relation between normalized relative thrust and convergence angle is statistically significant within this range.

4.4 Conclusions

The experimental data suggested that increasing collector electrode thickness reduces net thrust, as the penalty of parasitic drag outweighs any potential gains in ion collection area. Experimental results contradicted the hypotheses for camber and convergence angle, with both parameters showing a negative correlation with performance. These findings indicate that for annular EHD geometries, prioritizing frontal area reduction is more effective than attempting to leverage geometric shaping for neutral exhaust acceleration. At the characteristic low Reynolds numbers ($1500 < Re < 8000$), the airflow remains in the transitional regime where thicker profiles and aggressive geometries incur substantial drag. In the context of the simplified governing equation derived in the theoretical framework,

$$F_{net} = \frac{Id}{\mu}\left(1 - \frac{C_D A_f}{2A}\right) \tag{24}$$

minor adjustments to the electrostatic configuration or local electric field distribution caused by altering the collector shape were strongly offset by the increase in the non-dimensional drag penalty term, $\frac{C_D A_f}{2A}$. Consequently, aerodynamic optimization for minimum profile and form drag remain the primary design priority for EHD collector optimization.

5 Discussion

5.1 Aerodynamic–Electrostatic Tradeoff at Low Reynolds Numbers

The tested configurations operate within a moderate Reynolds number regime ($1500 < Re < 8000$), where both inertial and viscous effects contribute to aerodynamic behavior. In this range, bluff-body drag remains strongly dependent on frontal area and characteristic length. Increasing electrode thickness enhances ion collection area and electrostatic interaction; however, it also increases projected frontal area and therefore aerodynamic drag. The scaling relationship derived in this study indicates that electrostatic gains from increased collection surface grow slower than the aerodynamic penalty associated with increased thickness. Accordingly, thicker electrodes do not produce improved net thrust performance under these flow conditions. These results demonstrate that aerodynamic considerations impose a stronger constraint on electrode geometry than electrostatic surface maximization in small-scale EHD systems.

5.2 Experiment Limitations and Potential Sources of Error

Several potential sources of systemic and environmental error may have introduced marginal variance into the experimental results. Mechanical resistance within the ball bearing likely exerted an influence on force distribution. The precision of data acquisition may have been impacted by load cell drift, a common phenomenon where sensor output fluctuates over time due to prolonged strain or internal heating. This was mitigated through a new baseline reference for each test in the 30-second testing window. Environmental factors also present challenges; fluctuations in ambient humidity and temperature may alter the dielectric strength of air and corona discharge stability. Similarly, inconsistent internal wind currents within the testing facility may introduce lateral forces. Although these sources of error were monitored, they remain considerations for future refinement and calibration.

5.3 Potential Applications and Scaling

The optimization of thrust density and power efficiency provides a potential framework for transitioning EHD technology from specialized laboratory setups to potential atmospheric propulsion systems. By eliminating the mechanical complexities and moving parts inherent in rotary propulsion, optimized EHD thrusters offer a solid-state alternative with advantages in several thrust-critical domains.

5.3.1 Ozone Replenishment and HAPS

The utilization of optimized EHD actuators presents a potential propulsion alternative for High-Altitude Pseudo-Satellites (HAPS) operating within the lower stratosphere. At altitudes approaching 20 kilometers, the reduction in atmospheric density significantly diminishes aerody-

namic drag, which partially offsets the lower thrust-to-power ratios characteristic of ionic wind generation in rarefied media. In this environment, EHD systems may provide low-magnitude thrust required for the persistent station-keeping of solar-electric gliders and lighter-than-air communication platforms. A chemical consequence of the electrical ionization of air through corona discharge is the formation of triatomic oxygen, or ozone (O_3), as a dilute byproduct. Unlike conventional chemical propulsion systems that emit nitrogen oxides (NO_x) and water vapor—compounds known to catalyze the depletion of stratospheric ozone—the EHD process yields an exhaust profile that is chemically congruent with the existing atmospheric composition. While the volumetric output of ozone from a decentralized fleet of HAPS is negligible relative to the multi-billion ton annual production cycle driven by solar photochemistry, it represents an ecological alternative to traditional aviation emissions. The deployment of EHD-driven HAPS presents a dual-purpose role where the propulsion mechanism maintains the integrity of the stratospheric chemical environment. In this framework, the generation of ozone is classified as a secondary byproduct benefit that avoids the introduction of anthropogenic pollutants, ensuring that the act of maintaining persistent telecommunications infrastructure does not compromise the protective utility of the ozone layer.

5.3.2 Acoustically Stealthy UAVs

The near-silent acoustic profile of optimized EHD systems makes them applicable to stealth Uncrewed Aerial Vehicles (UAVs) and environmental monitoring drones. Because these systems minimize the acoustic footprint by removing the broadband noise of spinning blades, they allow for covert surveillance or non-disruptive wildlife observation in noise-sensitive ecosystems. Unlike traditional battery-powered propellers, these ion-driven systems may offer a higher degree of mechanical reliability due to the total absence of rotating parts and frictional wear.

5.3.3 Micro-Scale Robotics

Furthermore, the thrust-to-weight advantages of EHD systems scale well at the micro-level. As vehicle size decreases thrust density remains constant, causing thrust to scale with the square of the characteristic length, while mass scales with the cube of the characteristic length, proportional to the volume of the vehicle. This scaling law can permit a higher thrust-to-weight ratio in small-scale applications. This makes optimized EHD propulsion a potential candidate for insect-scale micro-robotics, where traditional electromagnetic motors are often too heavy or mechanically inefficient to sustain autonomous flight. However, as the distance between electrodes decreases, the thruster is more prone to the dielectric breakdown of air and an increased corona onset voltage. The thrust-to-power ratio of the thruster will also decrease, as more current is required to sustain constant thrust as electrode gap decreases due to Paschen's law. This suggests that the primary problem for EHD-driven micro-scale robotics is likely to

be power storage.

5.4 Future Work

By identifying that aerodynamic drag reduction is a primary driver of thrust in annular collectors, this research may inform the development of a new generation of high-efficiency, solid-state propulsion systems. The transition from a single-stage to a multistage EHD thruster introduces complex fluid-structure interactions, meaning that future experiments may investigate how the wake and ionized plume from initial stages affect the potential gradient and pressure distribution of subsequent stages. Potential future research applications may include focusing ionic wind into a coherent jet to minimize radial losses and determining the effects of intermediate stage geometries on net thrust. Annular airfoil collector geometries remain undercharacterized, and this study provides a preliminary dataset for future optimization.

References

Calvo, E. M., Pinheiro, M. J., & Sá, P. A. (2022). Modeling of electrohydrodynamic (ehd) plasma thrusters: Optimization of physical and geometrical parameters. *Applied Sciences*.

Drew, D. S., & Pister, K. S. J. (2017). Geometric optimization of microfabricated silicon electrodes for corona discharge-based electrohydrodynamic thrusters. *Micromachines*, *8*(5), 141. doi: 10.3390/mi8050141

Fei, L., Lin, Q., Bi, X., Chan, L., Chen, S., Yan, X., ... Cen, C. (2019, September). Geometric optimization of microfabricated silicon electrodes for corona discharge-based electrohydrodynamic thrusters. *Atmospheric Pollution Research*, *10*(5), 1435–1442. Retrieved from `http://dx.doi.org/10.1016/j.apr.2019.03.015` doi: 10.1016/j.apr.2019.03.015

Gilmore, C., & Barrett, S. (2015). Electrohydrodynamic thrust density using positive corona-induced ionic winds for in-atmosphere propulsion. *Proceedings of the Royal Society A*, *471*. doi: 10.1098/rspa.2014.0912

Hare, B., Scholten, O., Dwyer, J., Ebert, U., Nijdam, S., Bonardi, A., ... Winchen, T. (2020, March). Radio emission reveals inner meter-scale structure of negative lightning leader steps. *Physical Review Letters*, *124*(10). Retrieved from `http://dx.doi.org/10.1103/PhysRevLett.124.105101` doi: 10.1103/physrevlett.124.105101

Kahol, O., Belan, M., Pacchiani, M., & Montenero, D. (2023). Scaling relations for the geometry of wire-to-airfoil atmospheric ionic thrusters. *Journal of Electrostatics*.

Liu, G., Yuan, P., An, T., Cen, J., & Wang, X. (2019, August). A visible channel core and the channel structure below the connection point for natural cloud-to-ground light-

ning. *Applied Physics Letters*, *115*(6). Retrieved from http://dx.doi.org/10.1063/1.5111845 doi: 10.1063/1.5111845

Masuyama, K. (2012). *Performance characterization of electrohydrodynamic propulsion devices* (Tech. Rep.). Massachusetts Institute of Technology.

Neubert, T., Østgaard, N., Reglero, V., Chanrion, O., Heumesser, M., Dimitriadou, K., ... Eyles, C. J. (2020, January). A terrestrial gamma-ray flash and ionospheric ultraviolet emissions powered by lightning. *Science*, *367*(6474), 183–186. Retrieved from http://dx.doi.org/10.1126/science.aax3872 doi: 10.1126/science.aax3872

Schumann, U., & Huntrieser, H. (2007, July). The global lightning-induced nitrogen oxides source. *Atmospheric Chemistry and Physics*, *7*(14), 3823–3907. Retrieved from http://dx.doi.org/10.5194/acp-7-3823-2007 doi: 10.5194/acp-7-3823-2007

WANG, F., MA, X., CHEN, H., & ZHANG, Y. (2018, May). Evolution simulation of lightning discharge based on a magnetohydrodynamics method. *Plasma Science and Technology*, *20*(7), 075301. Retrieved from http://dx.doi.org/10.1088/2058-6272/aab841 doi: 10.1088/2058-6272/aab841

Wang, Y., DeSilva, A. W., Goldenbaum, G. C., & Dickerson, R. R. (1998, August). Nitric oxide production by simulated lightning: Dependence on current, energy, and pressure. *Journal of Geophysical Research: Atmospheres*, *103*(D15), 19149–19159. Retrieved from http://dx.doi.org/10.1029/98JD01356 doi: 10.1029/98jd01356

Xu, H., He, Y., Strobel, K. L., Gilmore, C. K., Kelley, S. P., Hennick, C. C., ... Barrett, S. R. H. (2018, November). Flight of an aeroplane with solid-state propulsion. *Nature*, *563*(7732), 532–535. Retrieved from http://dx.doi.org/10.1038/s41586-018-0707-9 doi: 10.1038/s41586-018-0707-9